

APPLIED SCIENCES AND ENGINEERING

Machine-knitted washable sensor array textile for precise epidermal physiological signal monitoring

Wenjing Fan¹, Qiang He¹, Keyu Meng¹, Xulong Tan¹, Zhihao Zhou¹, Gaoqiang Zhang¹, Jin Yang^{1*}, Zhong Lin Wang^{2,3*}

Wearable textile electronics are highly desirable for realizing personalized health management. However, most reported textile electronics can either periodically target a single physiological signal or miss the explicit details of the signals, leading to a partial health assessment. Furthermore, textiles with excellent property and comfort still remain a challenge. Here, we report a triboelectric all-textile sensor array with high pressure sensitivity and comfort. It exhibits the pressure sensitivity (7.84 mV Pa^{-1}), fast response time (20 ms), stability ($>100,000$ cycles), wide working frequency bandwidth (up to 20 Hz), and machine washability (>40 washes). The fabricated TATSAs were stitched into different parts of clothes to monitor the arterial pulse waves and respiratory signals simultaneously. We further developed a health monitoring system for long-term and noninvasive assessment of cardiovascular disease and sleep apnea syndrome, which exhibits great advancement for quantitative analysis of some chronic diseases.

INTRODUCTION

Wearable electronics represent a fascinating opportunity because of their promising applications in personalized medicine. They can monitor an individual's state of health in a continuous, real-time, and noninvasive manner (1–11). Pulse and respiration, as two indispensable components of vital signs, can provide both an accurate assessment of the physiological state and remarkable insights into the diagnosis and prognosis of related diseases (12–21). To date, most wearable electronics for detecting subtle physiological signals are based on ultrathin substrates such as polyethylene terephthalate, polydimethylsiloxane, polyimide, glass, and silicone (22–26). A drawback of these substrates for use on the skin lies on their planar and rigid formats. As a result, tapes, Band-Aids, or other mechanical fixtures are required to establish a compact contact between wearable electronics and human skin, which can cause irritation and inconvenience during extended periods of use (27, 28). Moreover, these substrates have poor air permeability, resulting in discomfort when used for long-term, continuous health monitoring. To alleviate the aforementioned issues in health care, especially in daily usage, smart textiles offer a reliable solution. These textiles have the characteristics of softness, light weight, and breathability and, thus, the potential for realizing comfort in wearable electronics. In recent years, intensive endeavors have been devoted to develop textile-based systems in sensitive sensors, energy harvesting, and storage (29–39). In particular, successful research has been reported on optical fiber, piezoelectricity, and resistivity-based smart textiles applied in the monitoring of pulse and respiratory signals (40–43). However, these smart textiles typically have low sensitivity and a single monitoring parameter and cannot be manufactured on a large scale (table S1). In the case of pulse measurement, detailed information is difficult to capture because of the faint and rapid

fluctuation of pulse (e.g., its feature points), and thus, high sensitivity and appropriate frequency response performance are required.

In this study, we introduce a triboelectric all-textile sensor array (TATSA) with high sensitivity for epidermal subtle pressure capturing, knitted with conductive and nylon yarns in a full cardigan stitch. The TATSA can provide high pressure sensitivity (7.84 mV Pa^{-1}), fast response time (20 ms), stability ($>100,000$ cycles), wide working frequency bandwidth (up to 20 Hz), and machine washability (>40 washes). It is capable of integrating itself conveniently into clothes with discretion, comfort, and aesthetic appeal. Notably, our TATSA can be directly incorporated into different sites of the fabric that correspond to the pulse waves at the neck, wrist, fingertip, and ankle positions and to the respiratory waves in the abdomen and chest. To evaluate the excellent performance of the TATSA in real-time and remote health monitoring, we develop a personalized intelligent health monitoring system to continuously acquire and save physiological signals for the analysis of cardiovascular disease (CAD) and the assessment of sleep apnea syndrome (SAS).

RESULTS

Fabrication and design

As illustrated in Fig. 1A, two TATSAs were stitched into the cuff and chest of a shirt to enable the dynamic and simultaneous monitoring of the pulse and respiratory signals, respectively. These physiological signals were transmitted wirelessly to the intelligent mobile terminal application (APP) for further analysis of health status. Figure 1B shows the TATSA stitched into a piece of cloth, and the inset shows the enlarged view of the TATSA, which was knitted using the characteristic conductive yarn and commercial nylon yarn together in a full cardigan stitch. Compared with the fundamental plain stitch, the most common and basic knitting method, the full cardigan stitch was chosen because the contact between the loop head of the conductive yarn and the adjacent tuck stitch head of the nylon yarn (fig. S1) is a surface rather than a point contact, leading to a larger acting area for high triboelectric effect. To prepare the conductive yarn, we selected stainless steel as the fixed core fiber, and several pieces of one-ply Terylene yarns were twisted around

Copyright © 2020 The Authors, some rights reserved; exclusive licensee American Association for the Advancement of Science. No claim to original U.S. Government Works. Distributed under a Creative Commons Attribution NonCommercial License 4.0 (CC BY-NC).

¹Department of Optoelectronic Engineering, Key Laboratory of Optoelectronic Technology and Systems, Ministry of Education, Chongqing University, Chongqing 400044, P. R. China. ²School of Materials Science and Engineering, Georgia Institute of Technology, Atlanta, GA 30332, USA. ³Beijing Institute of Nanoenergy and Nanosystems, Chinese Academy of Sciences, Beijing 100083, P. R. China.

*Corresponding author. Email: yangjin@cqu.edu.cn (J.Y.); zhong.wang@mse.gatech.edu (Z.L.W.)

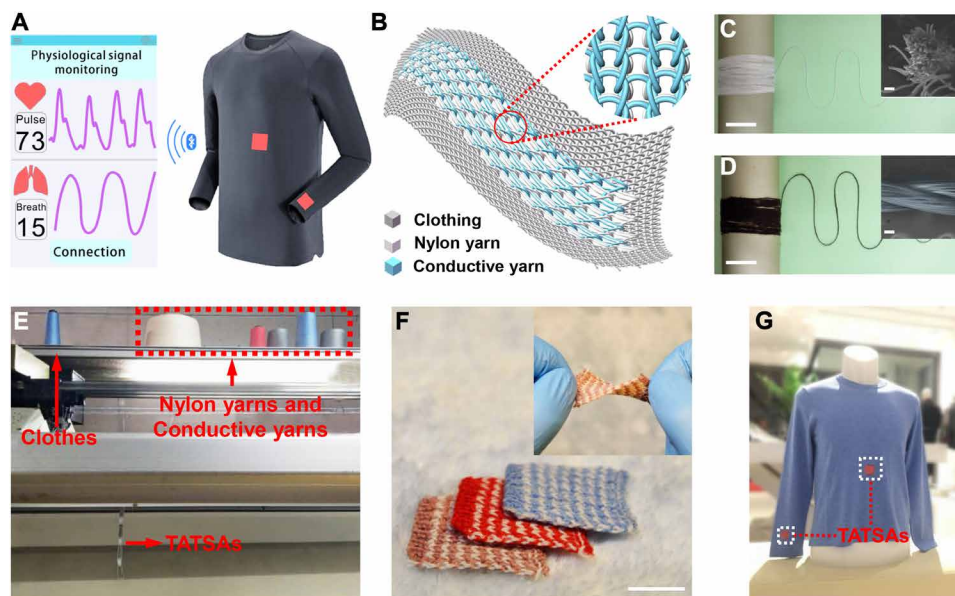


Fig. 1. Fabrication and structure of all-textile pressure sensors. (A) Two TATSAs integrated into a shirt for the monitoring of pulse and respiratory signals in real time. (B) Schematic illustration of the combination of TATSA and clothes. The inset shows the enlarged view of the sensor. (C) Photograph of the conductive yarn (scale bar, 4 cm). The inset is the SEM image of the cross section of the conductive yarn (scale bar, 100 μm), which consists of stainless steel and Terylene yarns. (D) Photograph of the nylon yarn (scale bar, 4 cm). The inset is the SEM image of the nylon yarn surface (scale bar, 100 μm). (E) Image of the computerized flat knitting machine carrying out the automatic weaving of the TATSAs. (F) Photograph of TATSAs in different colors (scale bar, 2 cm). The inset is the twisted TATSA, which demonstrates its excellent softness. (G) Photograph of two TATSAs completely and seamlessly stitched into a sweater. Photo credit: Wenjing Fan, Chongqing University.

the core fiber into one conductive yarn with a diameter of 0.2 mm (fig. S2), which served as both the electrification surface and the conducting electrode. The nylon yarn, which had a diameter of 0.15 mm and served as another electrification surface, had a strong tensile force because it was twisted by incomputable yarns (fig. S3). Figure 1 (C and D, respectively) shows photographs of the fabricated conductive yarn and nylon yarn. The insets show their respective scanning electron microscopy (SEM) images, which present a typical cross section of the conductive yarn and the surface of the nylon yarn. The high tensile strength of the conductive and nylon yarns ensured their weaving ability on an industrial machine to maintain a uniform performance of all sensors. As shown in Fig. 1E, the conductive yarns, nylon yarns, and ordinary threads were wound onto their respective cones, which were then loaded onto the industrial computerized flat knitting machine for automatic weaving (movie S1). As shown in fig. S4, several TATSAs were knitted together with ordinary cloth using the industrial machine. A single TATSA with a thickness of 0.85 mm and a weight of 0.28 g could be tailored from the entire structure for individual use, exhibiting its excellent compatibility with other cloths. In addition, TATSAs could be designed in various colors to meet aesthetic and fashionable requirements because of the diversity of commercial nylon yarns (Fig. 1F and fig. S5). The fabricated TATSAs have excellent softness and the capacity to withstand harsh bending or deformation (fig. S6). Figure 1G shows the TATSA stitched directly into the abdomen and cuff of a sweater. The process of knitting the sweater is shown in fig. S7 and movie S2. The details of the front and back side of the stretched TATSA at the abdomen position are shown in fig. S8 (A and B, respectively), and the position of conductive yarn and nylon yarn is illustrated in fig. S8C. It can be seen here that the TATSA can be embedded in ordinary fabrics seamlessly for a discreet and smart appearance.

Structure and working mechanism

To analyze the working mechanism of the TATSA, including its mechanical and electrical properties, we constructed a geometric knitting model of the TATSA, as shown in Fig. 2A. Using the full cardigan stitch, the conductive and nylon yarns are interlocked in forms of loop units in the course and wale direction. A single loop structure (fig. S1) consists of a loop head, loop arm, rib-crossing part, tuck stitch arm, and tuck stitch head. Two forms of the contact surface between the two different yarns can be found: (i) the contact surface between the loop head of the conductive yarn and the tuck stitch head of the nylon yarn and (ii) the contact surface between the loop head of the nylon yarn and the tuck stitch head of the conductive yarn.

The working principle of the TATSA can be explained in two aspects: external force stimulation and its induced charge. To intuitively understand the stress distribution in response to external force stimulus, we used finite element analysis using COMSOL software at different external forces of 2 and 0.2 kPa, as respectively shown in Fig. 2B and fig. S9. The stress appears on the contact surfaces of two yarns. As shown in fig. S10, we considered two loop units to clarify the stress distribution. In comparing the stress distribution under two different external forces, the stress on the surfaces of the conductive and nylon yarns increases with the increased external force, resulting in the contact and extrusion between the two yarns. Once the external force is released, the two yarns separate and move away from each other.

The contact-separation movements between the conductive yarn and nylon yarn induce charge transfer, which is attributed to the conjunction of triboelectrification and electrostatic induction. To clarify the electricity-generating process, we analyze the cross section of the area where the two yarns contact with each other (Fig. 2C₁). As demonstrated in Fig. 2 (C₂ and C₃, respectively),

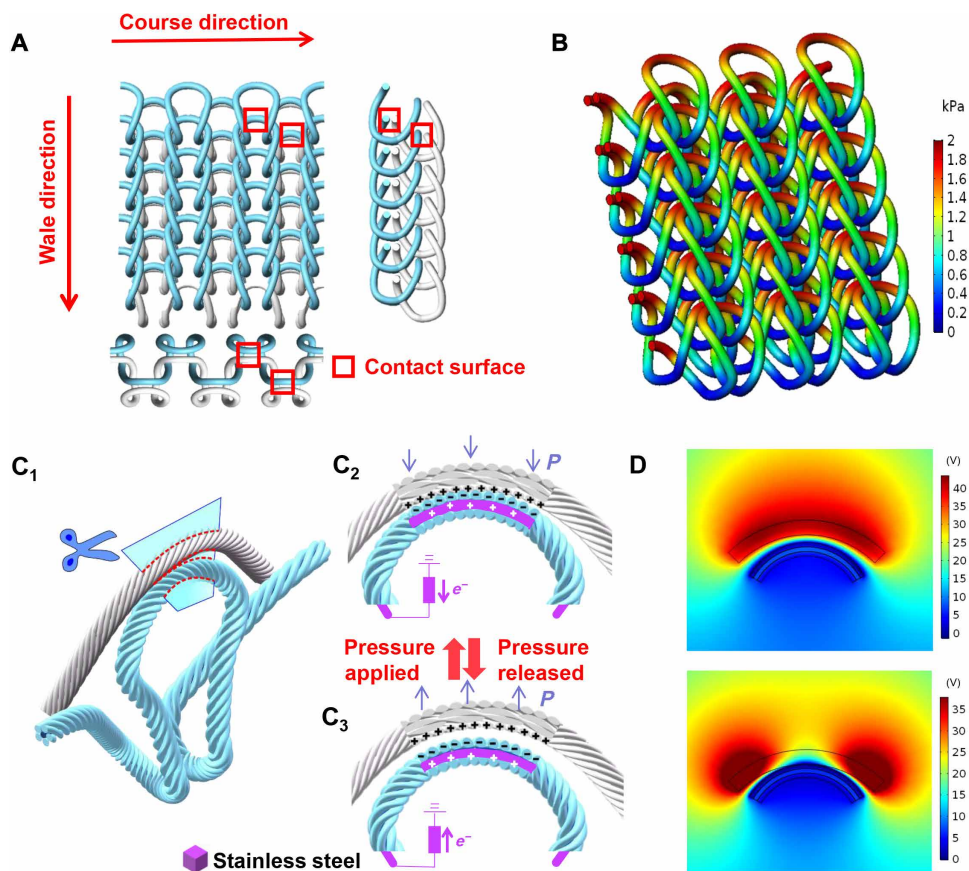


Fig. 2. Demonstration of the working principle of TATSA. (A) The TATSA with the front, right, and top sides of the knit loops. (B) Simulation result of the force distribution of a TATSA under an applied pressure of 2 kPa using the COMSOL software. (C) Schematic illustrations of the charge transfer of a contact unit under short-circuit conditions. (D) Simulation results of the charge distribution of a contact unit under an open circuit condition using the COMSOL software.

when the TATSA is stimulated by the external force and the two yarns contact with each other, electrification occurs on the surface of the conductive and nylon yarns, and the equivalent charges with opposite polarities are generated on the surface of the two yarns. Once the two yarns separate, positive charges are induced in the inner stainless steel because of the electrostatic induction effect. The complete schematic is shown in fig. S11. To acquire a more quantitative understanding of the electricity-generating process, we simulated the potential distribution of the TATSA using COMSOL software (Fig. 2D). When the two materials are in contact, the charge mainly collects on the friction material, and only a small amount of induced charge is present on the electrode, resulting in the small potential (Fig. 2D, bottom). When the two materials are separated (Fig. 2D, top), the induced charge on the electrode increases because of the potential difference, and the corresponding potential increases, which reveals a good accordance between the results obtained from the experiments and those from the simulations. Furthermore, since the conducting electrode of the TATSA is wrapped in Terylene yarns and the skin is in contact with both the two friction materials, therefore, when the TATSA is worn directly to the skin, the charge is dependent on the external force and will not be weakened by the skin.

Characterization of the TATSA

To characterize the performance of our TATSA in various aspects, we provided a measuring system containing a function generator,

power amplifier, electrodynamic shaker, force gauge, electrometer, and computer (fig. S12). This system generates an external dynamic pressure of up to 7 kPa. In experiment, the TATSA was placed on a flat plastic sheet in a free state, and the output electrical signals are recorded by the electrometer.

The specifications of the conductive and nylon yarns affect the output performance of the TATSA because they determine the contact surface and capacity for perceiving the external pressure. To investigate this, we fabricated three sizes of the two yarns, respectively: conductive yarn with a size of 150D/3, 210D/3, and 250D/3 and nylon yarn with a size of 150D/6, 210D/6, and 250D/6 (D, denier; a unit of measurement used to determine the fiber thickness of individual threads; fabrics with a high denier count tend to be thick). Then, we selected these two yarns with different sizes to knit them into a sensor, and the dimension of the TATSA was kept at 3 cm by 3 cm with the loop number of 16 in the wale direction and 10 in the course direction. Thus, the sensors with nine knitting patterns were obtained. The sensor by the conductive yarn with the size of 150D/3 and nylon yarn with the size of 150D/6 was the thinnest, and the sensor by the conductive yarn with the size of 250D/3 and nylon yarn with the size of 250D/6 was the thickest. Under a mechanical excitation of 0.1 to 7 kPa, the electrical outputs for these patterns were systematically investigated and tested, as shown in Fig. 3A. The output voltages of the nine TATSAs increased with the increased applied pressure, from 0.1 to 4 kPa. Specifically, of all the

knitting patterns, the specification of the 210D/3 conductive yarn and 210D/6 nylon yarn delivered the highest electrical output and exhibited the highest sensitivity. The output voltage showed an increasing trend with the increase in the thickness of the TATSA (because of the sufficient contact surface) until the TATSA was knitted using the 210D/3 conductive yarn and 210D/6 nylon yarn. As further increases in thickness would lead to the absorption of external pressure by the yarns, the output voltage decreased accordingly. Furthermore, it is noted that in the low-pressure region (<4 kPa), a well-behaved linear variation in the output voltage with pressure gave a superior pressure sensitivity of 7.84 mV Pa $^{-1}$. In the high-pressure region (>4 kPa), a lower pressure sensitivity of 0.31 mV Pa $^{-1}$ was experimentally observed because of the saturation of the effective friction area. A similar pressure sensitivity was demonstrated during the opposite process of applying force. The concrete time profiles of the output voltage and current under different pressures are presented in fig. S13 (A and B, respectively).

The sensitivity and output voltage were also influenced by the stitch density of the TATSA, which was determined by the total number of loops in a measured area of fabric. An increase in the stitch density would lead to the greater compactness of the fabric structure. Figure 3B shows the output performances under different loop numbers in the textile area of 3 cm by 3 cm, and the inset illustrates the structure of a loop unit (we kept the loop number in the course direction at 10, and the loop number in the wale direction was 12, 14, 16, 18, 20, 22, 24, and 26). By increasing the loop number, the output voltage first exhibited an increasing trend because of the increasing contact surface, until the maximum output voltage peak of 7.5 V with a loop number of 180. After this point, the output voltage followed a decreasing trend because the TATSA became tight, and the two yarns had a reduced contact-separation space. To explore in which direction the density has a great impact on the output, we kept the loop number of the TATSA in the wale direction at 18, and the loop number in the course direction was set to be

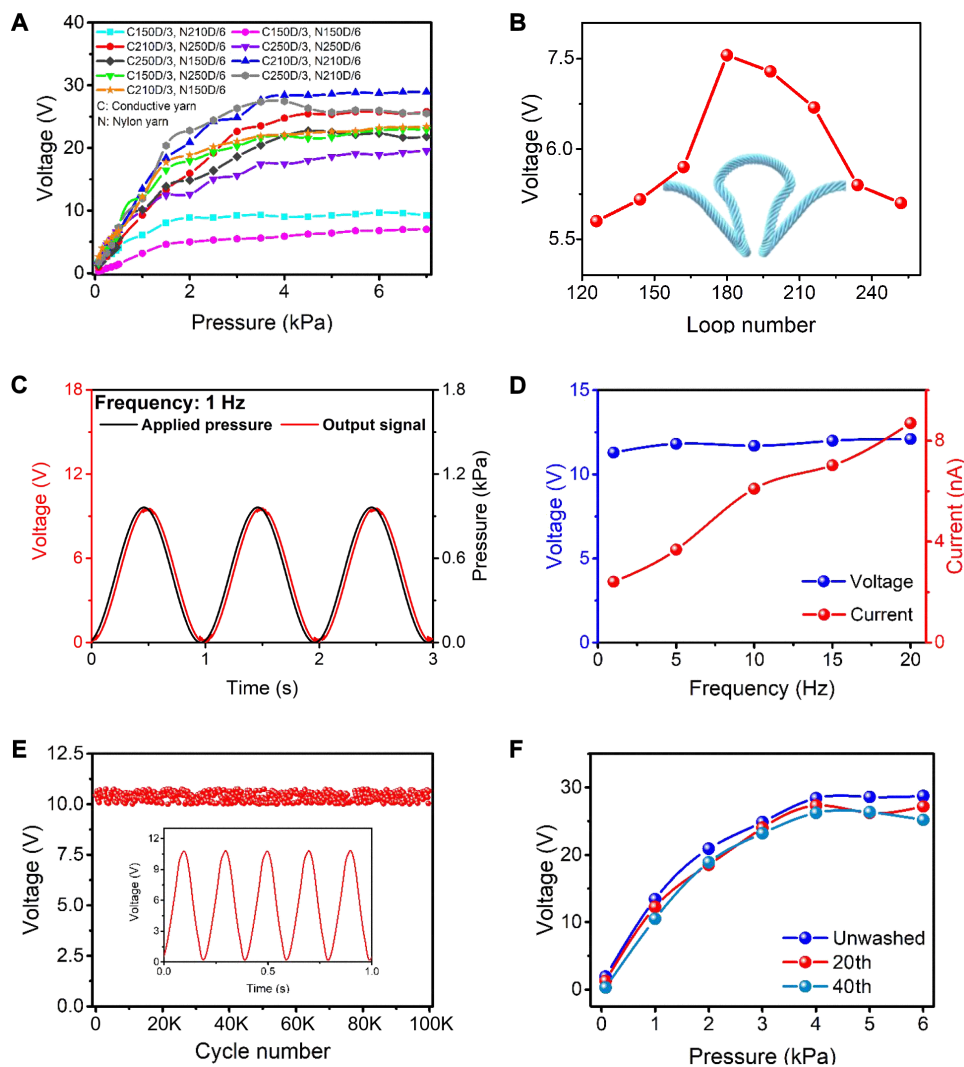


Fig. 3. Performance of the TATSA. (A) Output voltage under nine knitting patterns of the conductive yarn (150D/3, 210D/3, and 250D/3) combined with the nylon yarn (150D/6, 210D/6, and 250D/6). (B) Voltage response to various numbers of loop units in the same fabric area when keeping the loop number in the wale direction unchanged. (C) Plots showing the frequency responses under a dynamic pressure of 1 kPa and pressure input frequency of 1 Hz. (D) Different output and current voltages under the frequencies of 1, 5, 10, and 20 Hz. (E) Durability test of a TATSA under a pressure of 1 kPa. (F) Output characteristics of the TATSA after washing 20 and 40 times.

7, 8, 9, 10, 11, 12, 13, and 14. The corresponding output voltages are shown in fig. S14. By comparison, we can see that the density in the course direction has a greater influence on the output voltage. As a result, the knitting pattern of the 210D/3 conductive yarn and 210D/6 nylon yarn and 180 loop units were chosen to knit the TATSA after comprehensive evaluations of the output characteristics. Furthermore, we compared the output signals of two textile sensors using the full cardigan stitch and plain stitch. As shown in fig. S15, the electrical output and sensitivity using full cardigan stitch are much higher than that using plain stitch.

The response time for monitoring real-time signals was measured. To examine the response time of our sensor to external forces, we compared the output voltage signals with the dynamic pressure inputs at a frequency of 1 to 20 Hz (Fig. 3C and fig. S16, respectively). The output voltage waveforms were almost identical to the input sinusoidal pressure waves under a pressure of 1 kPa, and the output waveforms had a fast response time (about 20 ms). This hysteresis may be attributed to the elastic structure not having returned to the original state as soon as possible after receiving the external force. Nevertheless, this tiny hysteresis is acceptable for real-time monitoring. To obtain the dynamic pressure with a certain frequency range, an appropriate frequency response of TATSA is expected. Thus, the frequency characteristic of TATSA was also tested. By increasing the external exciting frequency, the amplitude of the output voltage remained almost unchanged, whereas the amplitude of the current increased when the tapping frequencies varied from 1 to 20 Hz (Fig. 3D).

To evaluate the repeatability, stability, and durability of the TATSA, we tested the output voltage and current responses to pressure loading-unloading cycles. A pressure of 1 kPa with a frequency of 5 Hz was applied to the sensor. The peak-to-peak voltage and current were recorded after 100,000 loading-unloading cycles (Fig. 3E and fig. S17, respectively). The enlarged views of the voltage and the current waveform are shown in the inset of Fig. 3E and fig. S17, respectively. The results reveal the remarkable repeatability, stability, and durability of the TATSA. Washability is also an essential assessment criterion of the TATSA as an all-textile device. To evaluate the washing ability, we tested the output voltage of the sensor after we machine-washed the TATSA according to the American Association of Textile Chemists and Colorists (AATCC) Test Method 135-2017. The detailed washing procedure is described in Materials and Methods. As shown in Fig. 3F, the electrical outputs were recorded after washing 20 times and 40 times, which demonstrated that there were no distinct changes of the output voltage throughout the washing tests. These results verify the remarkable washability of the TATSA. As a wearable textile sensor, we also explored the output performance when the TATSA was in tensile (fig. S18), twisted (fig. S19), and different humidity (fig. S20) conditions.

Wireless mobile health monitoring system for arterial pulse and respiration monitoring

On the basis of the numerous advantages of the TATSA demonstrated above, we developed a wireless mobile health monitoring system (WMHMS), which has the capability of continuously acquiring physiological signals and then giving professional advice for a patient. Figure 4A shows the scheme diagram of the WMHMS based on the TATSA. The system has four components: the TATSA to acquire the analog physiological signals, an analog conditioning circuit with a low-pass filter (MAX7427) and an amplifier (MAX4465)

to ensure sufficient details and excellent synchronism of signals, an analog-to-digital converter based on a microcontroller unit to collect and convert the analog signals to digital signals, and a Bluetooth module (CC2640 low-power Bluetooth chip) to transmit the digital signal to the mobile phone terminal application (APP; Huawei Honor 9). In this study, we stitched the TATSA seamlessly into a lace, wristband, fingerstall, and sock, as shown in Fig. 4B.

To monitor the pulse signals of the different human body parts, we attached aforementioned decorations with TATSAs to the corresponding positions: neck (Fig. 4C₁), wrist (Fig. 4D₁), fingertip (Fig. 4E₁), and ankle (Fig. 4F₁), as elaborated in movies S3 to S6. In medicine, there are three substantial feature points in the pulse wave: the peak of the advancing wave P_1 , the peak of the reflected wave P_2 , and the peak of the dicrotic wave P_3 . The characteristics of these feature points reflect the health state of arterial elasticity, peripheral resistance, and left ventricular contractility related to the cardiovascular system. The pulse waveforms of a 25-year-old woman at the above four positions were acquired and recorded in our test. Note that the three distinguishable feature points (P_1 to P_3) were observed on the pulse waveform at the neck, wrist, and fingertip positions, as shown in Fig. 4 (C₂ to E₂). By contrast, only P_1 and P_3 appeared on the pulse waveform at the ankle position, and P_2 was not present (Fig. 4F₂). This result was caused by the superposition of the incoming blood wave ejected by the left ventricle and the reflected wave from the lower limbs (44). Prior studies have shown that P_2 presents in waveforms measured in the upper extremities but not in the ankle (45, 46). We observed similar results in the waveforms measured with the TATSA, as shown in fig. S21, which shows typical data from the population of 80 patients studied here. We can see that P_2 did not appear in these pulse waveforms measured in the ankle, demonstrating the ability of the TATSA to detect subtle features within the waveform. These pulse measurement results indicate that our WMHMS can accurately reveal the pulse wave characteristics of the upper and lower body and that it is superior to other works (41, 47). To further indicate that our TATSA can be widely applied to different ages, we measured pulse waveforms of 80 subjects at different ages, and we showed some typical data, as shown in fig. S22. As shown in Fig. 4G, we chose three participants aged 25, 45, and 65 years old, and the three feature points were obvious for the young and middle-aged participants. According to the medical literature (48), the characteristics of most people's pulse waveforms change as they age, such as the disappearance of the point P_2 , which is caused by the reflected wave moved forward to superimpose itself on the advancing wave through the decrease in vascular elasticity. This phenomenon is also reflected in the waveforms that we collected, further verifying that the TATSA can be applied to different populations.

Pulse waveform is affected not only by the physiological state of the individual but also by the test conditions. Therefore, we measured the pulse signals under different contact tightness between the TATSA and the skin (fig. S23) and various detecting positions at the measuring site (fig. S24). It can be found that the TATSA can obtain consistent pulse waveforms with detailed information around the vessel in a large effective detecting area at the measuring site. In addition, there are distinct output signals under different contact tightness between the TATSA and the skin. In addition, the motion of individuals wearing the sensors would affect the pulse signals. When the wrist of the subject is in a static condition, the amplitude of the obtained pulse waveform is stable (fig. S25A); conversely,

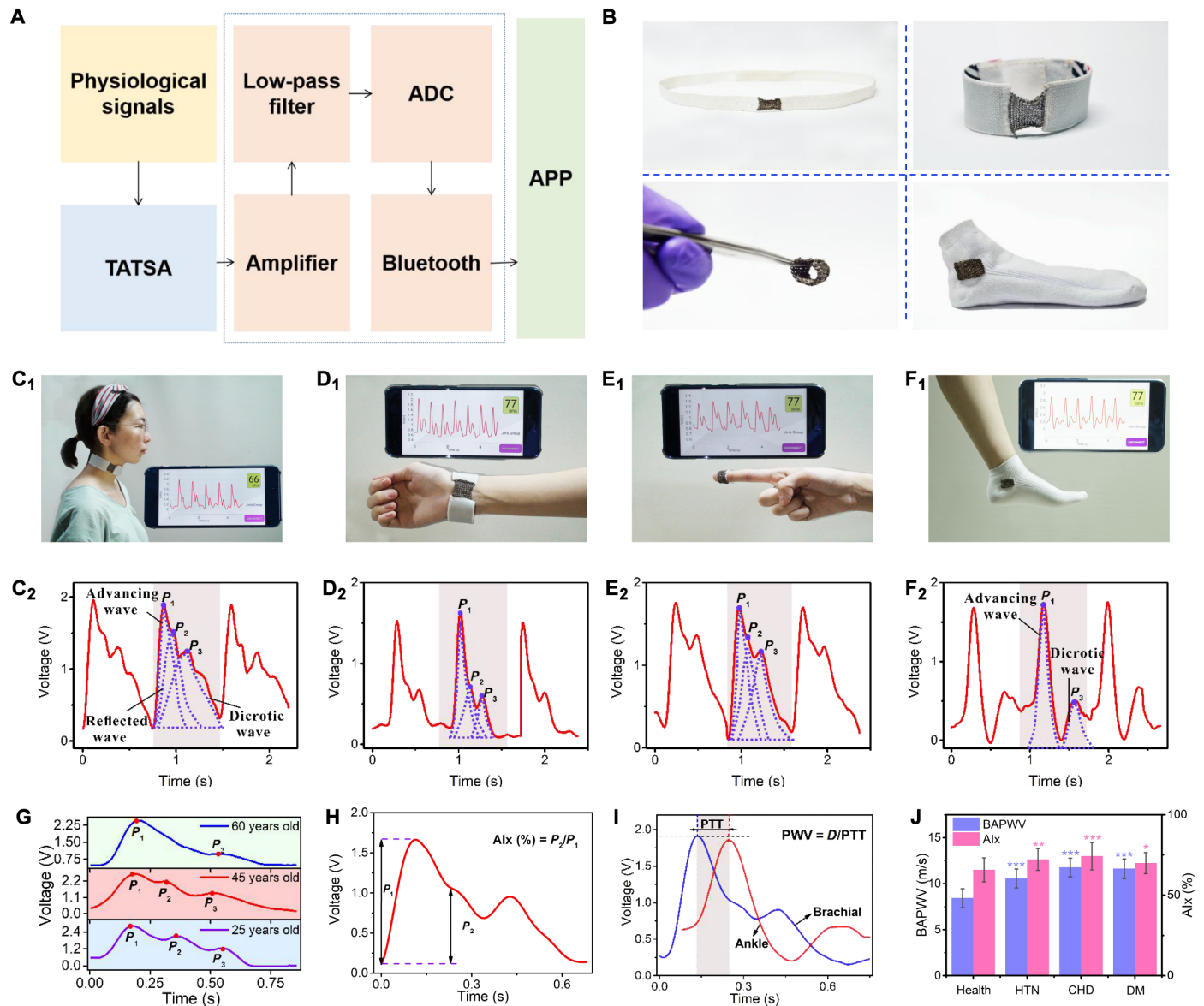


Fig. 4. Pulse wave measurements at various artery positions and analysis of the pulse signals. (A) Illustration of the WMHMS. (B) Photographs of the TATSAs stitched into a wristband, fingerstall, sock, and chest strap, respectively. Measurement of the pulse at the (C₁) neck, (D₁) wrist, (E₁) fingertip, and (F₁) ankle. Pulse waveform at the (C₂) neck, (D₂) wrist, (E₂) fingertip, and (F₂) ankle. (G) Pulse waveforms of different ages. (H) Analysis of a single pulse wave. Radial augmentation index (Alx) defined as $Alx (\%) = P_2/P_1$. P_1 is the peak of the advancing wave, and P_2 is the peak of the reflected wave. (I) A pulse cycle of the brachial and the ankle. Pulse wave velocity (PWV) is defined as $PWV = D/\Delta T$. D is the distance between the peaks of the ankle and brachial pulse waves. ΔT is the time delay between the peaks of the ankle and brachial pulse waves. PTT, pulse transit time. (J) Comparison of Alx and brachial-ankle PWV (BAPPW) between healthy and CADs. * $P < 0.01$, ** $P < 0.001$, and *** $P < 0.05$. HTN, hypertension; CHD, coronary heart disease; DM, diabetes mellitus. Photo credit: Jin Yang, Chongqing University.

when the wrist is slowly moving at an angle from -70° to 70° during 30 s, the amplitude of the pulse waveform will fluctuate (fig. S25B). However, the contour of each pulse waveform is visible, and the pulse rate can still be accurately obtained. Obviously, to achieve stable pulse wave acquisition in human motion, further work including sensor design and back-end signal processing is needed to be researched.

Furthermore, to analyze and quantitatively assess the condition of the cardiovascular system through the acquired pulse waveforms using our TATSA, we introduced two hemodynamic parameters

according to the assessment specification of the cardiovascular system, namely, the augmentation index (Alx) and the pulse wave velocity (PWV), which represent the elasticity of arteries. As shown in Fig. 4H, the pulse waveform at the wrist position of the 25-year-old healthy man was used for the analysis of Alx. According to the formula (section S1), $Alx = 60\%$ was obtained, which is a normal value. Then, we simultaneously collected two pulse waveforms at the arm and ankle positions of this participant (the detailed method of measuring of the pulse waveform is described in Materials and Methods). As shown in Fig. 4I, the feature points of the two pulse waveforms

were distinct. We then calculated the PWV according to the formula (section S1). $PWV = 1363 \text{ cm/s}$, which is a characteristic value expected of a healthy adult male, was obtained. On the other hand, we can see that the metrics of AIx or PWV is not affected by the amplitude difference of the pulse waveform, and the values of AIx in different body parts are various. In our study, the radial AIx was used. To verify the applicability of WMHMS in different people, we selected 20 participants in the healthy group, 20 in the hypertension (HTN) group, 20 in the coronary heart disease (CHD) group aged from 50 to 59 years old, and 20 in the diabetes mellitus (DM) group. We measured their pulse waves and compared their two parameters, AIx and PWV, as presented in Fig. 4J. It can be found that the PWV values of the HTN, CHD, and DM groups were lower compared with that of healthy group and have statistical difference ($P_{HTN} \ll 0.001$, $P_{CHD} \ll 0.001$, and $P_{DM} \ll 0.001$; the P values were calculated by t test). Meanwhile, the AIx values of the HTN and CHD groups were lower compared with the healthy group and have statistical difference ($P_{HTN} < 0.01$, $P_{CHD} < 0.001$, and $P_{DM} < 0.05$). The PWV and AIx of the participants with CHD, HTN, or DM were higher than those in the healthy group. The results show that the TATSA is

capable of accurately obtaining the pulse waveform to calculate the cardiovascular parameter to assess cardiovascular health status. In conclusion, because of its wireless, high-resolution, high-sensitivity characteristics and comfort, the WMHMS based on the TATSA provides a more efficient alternative for real-time monitoring than the current expensive medical equipment used in hospitals.

Aside from the pulse wave, respiratory information is also a primary vital sign to help assess the physical condition of an individual. The monitoring of respiration based on our TATSA is more attractive than the conventional polysomnography because it can be seamlessly integrated into clothes for better comfort. Stitched into a white elastic chest strap, the TATSA was directly tied to the human body and secured around the chest for monitoring respiration (Fig. 5A and movie S7). The TATSA deformed with the expansion and contraction of the ribcage, resulting in an electrical output. The acquired waveform is verified in Fig. 5B. The signal with large fluctuations (an amplitude of 1.8 V) and periodic changes (a frequency of 0.5 Hz) corresponded to the respiratory motion. The relatively small fluctuation signal was superimposed on this large fluctuation signal, which was the heartbeat signal. According to the frequency characteristics

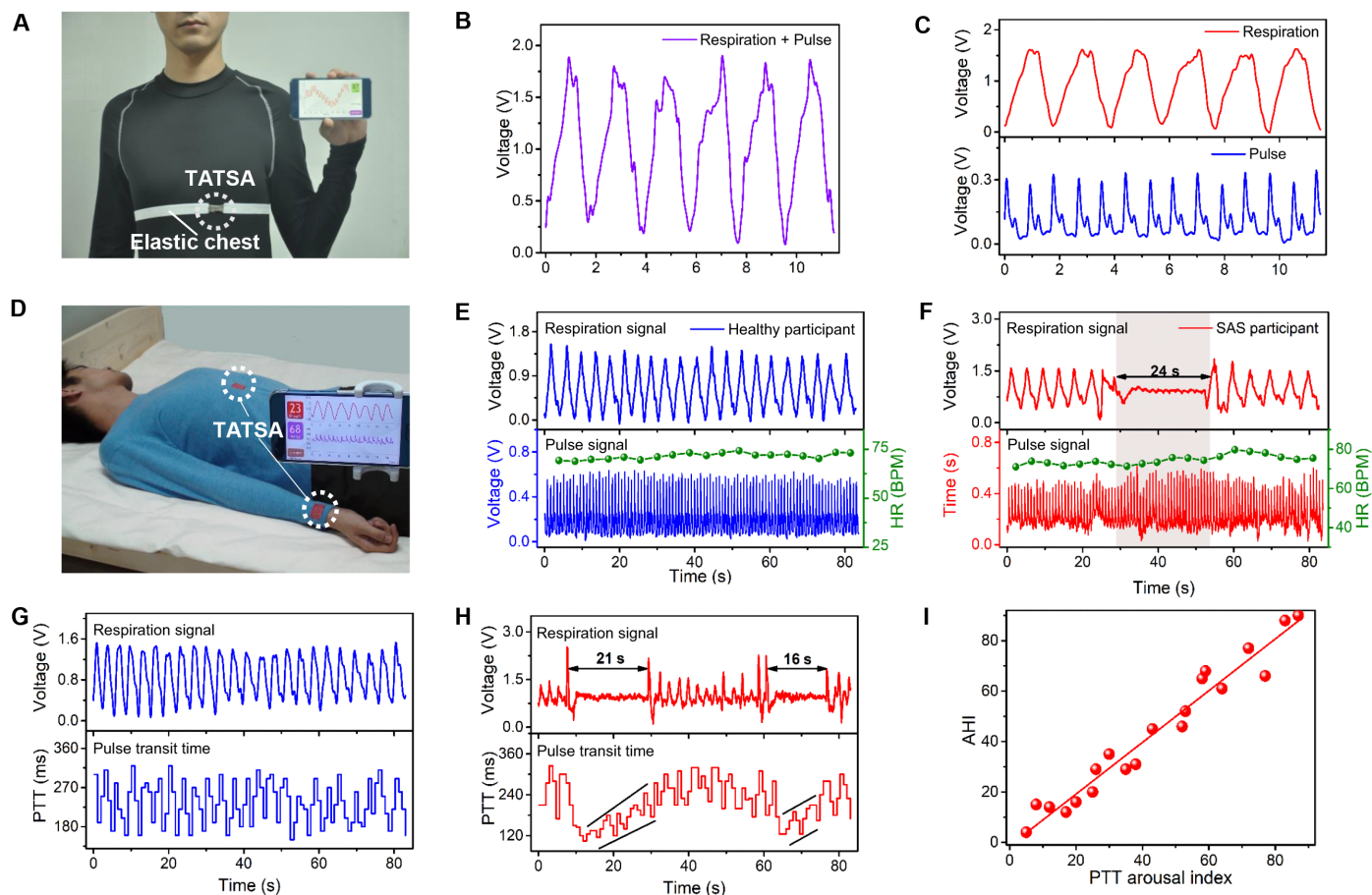


Fig. 5. Respiratory wave measurements and analysis of SAS. (A) Photograph showing the display of the TATSA placed on the chest for measuring the signal in the pressure associated with respiration. (B) Voltage-time plot for the TATSA mounted on the chest. (C) Decomposition of the signal (B) into the heartbeat and the respiratory waveform. (D) Photograph showing two TATSAs placed on the abdomen and wrist for measuring respiration and pulse, respectively, during sleep. (E) Respiratory and pulse signals of a healthy participant. HR, heart rate; BPM, beats per minute. (F) Respiratory and pulse signals of a SAS participant. (G) Respiratory signal and PTT of a healthy participant. (H) Respiratory signal and PTT of a SAS participant. (I) Relationship between PTT arousal index and apnea-hypopnea index (AHI). Photo credit: Wenjing Fan, Chongqing University.

of the respiration and heartbeat signals, we used a 0.8-Hz low-pass filter and a 0.8- to 20-Hz band-pass filter to separate the respiratory and heartbeat signals, respectively, as shown in Fig. 5C. In this case, stable respiratory and pulse signals with abundant physiological information (such as respiratory rate, heartbeat rate, and feature points of the pulse wave) were obtained simultaneously and accurately by simply placing the single TATSA on the chest.

To prove that our sensor can accurately and reliably monitor pulse and respiratory signals, we carried out an experiment to compare the measurement results of the pulse and respiration signals between our TATSAs and a standard medical instrument (MHM-6000B), as elaborated in movies S8 and S9. In pulse wave measurement, the photoelectric sensor of the medical instrument was worn on the left index finger of a young girl, and meanwhile, our TATSA was worn on her right index finger. From the two acquired pulse waveforms, we can see that their contours and details were identical, indicating that the pulse measured by the TATSA is as precise as that by the medical instrument. In respiration wave measurement, five electrocardiographic electrodes were attached to five areas on the body of a young man according to the medical instruction. In contrast, only one TATSA was directly tied to the body and secured around the chest. From the collected respiratory signals, it can be seen that the variation tendency and rate of the detected respiration signal by our TATSA were consistent with that by the medical instrument. These two comparison experiments validated the accuracy, reliability, and simplicity of our sensor system for monitoring pulse and respiratory signals.

Furthermore, we fabricated a piece of smart clothing and stitched two TATSAs at the abdomen and wrist positions for monitoring the respiratory and pulse signals, respectively. Specifically, a developed dual-channel WMHMS was used to capture the pulse and respiratory signals simultaneously. Through this system, we obtained the respiratory and pulse signals of a 25-year-old man dressed in our smart clothing while sleeping (Fig. 5D and movie S10) and sitting (fig. S26 and movie S11). The acquired respiratory and pulse signals could be wirelessly transmitted to the APP of the mobile phone. As mentioned above, the TATSA has the ability to capture respiratory and pulse signals. These two physiological signals are also the criteria to estimate SAS medically. Therefore, our TATSA can also be used to monitor and assess sleep quality and related sleep disorders. As shown in Fig. 5 (E and F, respectively), we continuously measured the pulse and respiratory waveforms of two participants, a healthy one and a patient with SAS. For the person without apnea, the measured respiratory and pulse rates remained stable at 15 and 70, respectively. For the patient with SAS, a distinct apnea for 24 s, which is an indication of an obstructive respiratory event, was observed, and the heart rate slightly increased after a period of apnea because of the regulation of the nervous system (49). In summary, respiratory status can be evaluated by our TATSA.

To further assess the type of SAS through pulse and respiratory signals, we analyzed the pulse transit time (PTT), a noninvasive indicator reflecting the changes in peripheral vascular resistance and intrathoracic pressure (defined in section S1) of a healthy man and a patient with SAS. For the healthy participant, the respiratory rate remained unchanged, and the PTT was relatively stable from 180 to 310 ms (Fig. 5G). However, for the SAS participant, the PTT increased continuously from 120 to 310 ms during apnea (Fig. 5H). Thus, the participant was diagnosed with obstructive SAS (OSAS). If the change in PTT decreased during the apnea, then the condition would be determined as a central sleep apnea syndrome (CSAS), and

if both of these two symptoms existed simultaneously, then it would be diagnosed as a mixed SAS (MSAS). To assess the severity of SAS, we further analyzed the collected signals. PTT arousal index, which is the number of PTT arousals per hour (PTT arousal is defined as a fall in PTT of ≥ 15 ms lasting for ≥ 3 s), plays a vital role in evaluating the degree of SAS. The apnea-hypopnea index (AHI) is a standard for determining the degree of SAS (apnea is the cessation of breathing, and hypopnea is overly shallow breathing or an abnormally low respiratory rate), which is defined as the number of apneas and hypopneas per hour while sleeping (the relationship between the AHI and the rating criteria for OSAS is shown in table S2). To investigate the relationship between the AHI and the PTT arousal index, the respiratory signals of 20 patients with SAS were selected and analyzed with TATSAs. As shown in Fig. 5I, the PTT arousal index positively correlated with the AHI, as apnea and hypopnea during sleep cause the obvious and transient elevation of blood pressure, leading to the decrease in the PTT. Therefore, our TATSA can obtain stable and accurate pulse and respiratory signals simultaneously, thus providing important physiological information on the cardiovascular system and SAS for the monitoring and evaluation of related diseases.

DISCUSSION

In summary, we developed a TATSA using the full cardigan stitch to detect different physiological signals simultaneously. This sensor featured a high sensitivity of 7.84 mV Pa^{-1} , fast response time of 20 ms, high stability of over 100,000 cycles, and wide working frequency bandwidth. On the basis of the TATSA, a WMHMS was also developed to transmit the measured physiological parameters to a mobile phone. TATSA can be incorporated into different sites of clothes for aesthetic design and used to simultaneously monitor the pulse and respiratory signals in real time. The system can be applied to help distinguish between healthy individuals and those with CAD or SAS because of its capability to capture detailed information. This study provided a comfortable, efficient, and user-friendly approach for measuring human pulse and respiration, representing an advancement in the development of wearable textile electronics.

MATERIALS AND METHODS

Fabrication of conductive yarn

The stainless steel was repeatedly passed through the mold and stretched to form a fiber with a diameter of 10 μm . A stainless steel fiber as the electrode was inserted into several pieces of commercial one-ply Terylene yarns.

Experimental setup for pressure and electrical characterization

A function generator (Stanford DS345) and an amplifier (LabworkPa-13) were used to provide a sinusoidal pressure signal. A dual-range force sensor (Vernier Software & Technology LLC) was used to measure the external pressure applied to the TATSA. A Keithley system electrometer (Keithley 6514) was used to monitor and record the output voltage and current of the TATSA.

Washing test

According to AATCC Test Method 135-2017, we used the TATSA and enough ballast as a 1.8-kg load and then put them into a commercial

laundrying machine (Labtex LBT-M6T) to perform delicate machine washing cycles. Then, we filled the laundrying machine with 18 gallons of water at 25°C and set the washer for the selected washing cycle and time (agitation speed, 119 strokes per minute; washing time, 6 min; final spin speed, 430 rpm; final spin time, 3 min). Last, the TATSA was hung dry in still air at room temperature not higher than 26°C.

Measurement of PWV

The subjects were instructed to lie in a supine position on the bed. The TATSA was placed on the measuring sites. Once the subjects were in standard supine position, they maintained a completely relaxed state for 5 to 10 min. The pulse signal then started measuring.

SUPPLEMENTARY MATERIALS

Supplementary material for this article is available at <http://advances.sciencemag.org/cgi/content/full/6/11/eaay2840/DC1>

Section S1. Definition of Alx and PWV

Fig. S1. A geometrical model for loop structure.

Fig. S2. Structure of the conductive yarn.

Fig. S3. Structure of the nylon thread.

Fig. S4. Compatibility of the TATSAs.

Fig. S5. Photograph of TATSAs in different colors.

Fig. S6. Photographs demonstrating that the TATSA has remarkable endurance.

Fig. S7. Computerized flat knitting machine carrying out automatic knitting of a cloth.

Fig. S8. Details of the TATSA.

Fig. S9. Simulation result of the force distribution of a TATSA under applied pressures at 0.2 kPa using the COMSOL software.

Fig. S10. Simulation results of the force distribution of a contact unit under the applied pressures at 0.2 and 2 kPa, respectively.

Fig. S11. Complete schematic illustrations of the charge transfer of a contact unit under short-circuit conditions.

Fig. S12. Schematic illustration of the experimental setup.

Fig. S13. Continuous output voltage and current of TATSA in response to the continuously applied external pressure in a measurement cycle.

Fig. S14. Voltage response to various numbers of loop units in the same fabric area when keeping the loop number in the wale direction unchanged.

Fig. S15. A comparison between the output performances of the two textile sensors using the full cardigan stitch and plain stitch.

Fig. S16. Plots showing frequency responses at the dynamic pressure of 1 kPa and pressure input frequency of 3, 5, 7, 9, 10, 11, 13, 15, 18, and 20 Hz.

Fig. S17. The durability test of a TATSA under a pressure of 1 kPa.

Fig. S18. The output voltages of the TATSA at different tension in the wale and course direction.

Fig. S19. The output voltages after different twisting times.

Fig. S20. The output voltages of the sensor at various relative humidity from 10 to 90%.

Fig. S21. The pulse waveforms at ankle of different individuals.

Fig. S22. The pulse waveforms of different age groups.

Fig. S23. Different tightness was achieved by tightening the wristbands at both ends of the sensor.

Fig. S24. The pulse waveforms on different measuring positions.

Fig. S25. The output voltages of the sensor when the subject was in the static and motion conditions.

Fig. S26. Photograph showing the TATSAs placed on the abdomen and wrist simultaneously for measuring respiration and pulse, respectively.

Table S1. Performances and applications of smart textiles for wearable devices.

Table S2. Data of Alx and PWV of the healthy, HTN, CHD, and DM groups.

Table S3. Rating criteria for OSAS.

Movie S1. Fabrication of the TATSA.

Movie S2. Fabrication of the clothes.

Movie S3. Monitoring of the pulse signal at the neck.

Movie S4. Monitoring of the pulse signal at the wrist.

Movie S5. Monitoring of the pulse signal at the fingertip.

Movie S6. Monitoring of the pulse signal at the ankle.

Movie S7. Monitoring of the pulse and respiratory signals at the chest.

Movie S8. Comparison of the pulse waveforms measured by the medical instrument and the TATSA.

Movie S9. Comparison of the respiratory waveforms measured by the medical instrument and the TATSA.

Movie S10. Monitoring of the pulse and respiratory signals while sleeping.

Movie S11. Monitoring of the pulse and respiratory signals while sitting.

[View/request a protocol for this paper from Bio-protocol.](#)

REFERENCES AND NOTES

1. S. Han, J. Kim, S. M. Won, Y. Ma, D. Kang, Z. Xie, K.-T. Lee, H. U. Chung, A. Banks, S. Min, S. Y. Heo, C. R. Davies, J. W. Lee, C.-H. Lee, B. H. Kim, K. Li, Y. Zhou, C. Wei, X. Feng, Y. Huang, J. A. Rogers, Battery-free, wireless sensors for full-body pressure and temperature mapping. *Sci. Transl. Med.* **10**, eaan4950 (2018).
2. L. Y. Chen, B. C.-K. Tee, A. L. Chortos, G. Schwartz, V. Tse, D. J. Lipomi, H.-S. P. Wong, M. V. McConnell, Z. Bao, Continuous wireless pressure monitoring and mapping with ultra-small passive sensors for health monitoring and critical care. *Nat. Commun.* **5**, 5028 (2014).
3. K.-I. Jang, H. N. Jung, J. W. Lee, S. Xu, Y. H. Liu, Y. Ma, J.-W. Jeong, Y. M. Song, J. Kim, B. H. Kim, A. Banks, J. W. Kwak, Y. Yang, D. Shi, Z. Wei, X. Feng, U. Paik, Y. Huang, R. Ghaffari, J. A. Rogers, Ferromagnetic, folded electrode composite as a soft interface to the skin for long-term electrophysiological recording. *Adv. Funct. Mater.* **26**, 7281–7290 (2016).
4. S. R. Krishnan, C.-J. Su, Z. Xie, M. Patel, S. R. Madhupathy, Y. Xu, J. Freudman, B. Ng, S. Y. Heo, H. Wang, T. R. Ray, J. Leshock, I. Stankiewicz, X. Feng, Y. Huang, P. Gutruf, J. A. Rogers, Epidermal electronics: Wireless, battery-free epidermal electronics for continuous, quantitative, multimodal thermal characterization of skin (*Small* 47/2018). *Small* **14**, 1870226 (2018).
5. Y. Liu, J. J. S. Norton, R. Qazi, Z. Zou, K. R. Ammann, H. Liu, L. Yan, P. L. Tran, K.-I. Jang, J. W. Lee, D. Zhang, K. A. Kilian, S. H. Jung, T. Bretl, J. Xiao, M. J. Slepian, Y. Huang, J.-W. Jeong, J. A. Rogers, Epidermal mechano-acoustic sensing electronics for cardiovascular diagnostics and human-machine interfaces. *Sci. Adv.* **2**, e1601185 (2016).
6. J. Reeder, M. Kaltenbrunner, T. Ware, D. Arreaga-Salas, A. Avendano-Bolivar, T. Yokota, Y. Inoue, M. Sekino, W. Voit, T. Sekitani, T. Someya, Mechanically adaptive organic transistors for implantable electronics. *Adv. Mater.* **26**, 4967–4973 (2014).
7. K. Kuribara, H. Wang, N. Uchiyama, K. Fukuda, T. Yokota, U. Zschieschang, C. Jaye, D. Fischer, H. Klauk, T. Yamamoto, K. Takimiya, M. Ikeda, H. Kuwabara, T. Sekitani, Y.-L. Loo, T. Someya, Organic transistors with high thermal stability for medical applications. *Nat. Commun.* **3**, 723 (2012).
8. J. Kim, P. Gutruf, A. M. Chiarelli, S. Y. Heo, K. Cho, Z. Xie, A. Banks, S. Han, K.-I. Jang, J. W. Lee, K.-T. Lee, X. Feng, Y. Huang, M. Fabiani, G. Gratton, U. Paik, J. A. Rogers, Miniaturized battery-free wireless systems for wearable pulse oximetry. *Adv. Funct. Mater.* **27**, 1604373 (2017).
9. R. A. Nawrocki, H. Jin, S. Lee, T. Yokota, M. Sekino, T. Someya, Self-adhesive and ultra-conformable, sub-300 nm dry thin-film electrodes for surface monitoring of biopotentials. *Adv. Funct. Mater.* **28**, 1803279 (2018).
10. S. Park, S. W. Heo, W. Lee, D. Inoue, Z. Jiang, K. Yu, H. Jinno, D. Hashizume, M. Sekino, T. Yokota, K. Fukuda, K. Tajima, T. Someya, Self-powered ultra-flexible electronics via nano-grating-patterned organic photovoltaics. *Nature* **561**, 516–521 (2018).
11. T. Yokota, Y. Inoue, Y. Terakawa, J. Reeder, M. Kaltenbrunner, T. Ware, K. Yang, K. Mabuchi, T. Murakawa, M. Sekino, W. Voit, T. Sekitani, T. Someya, Ultraflexible, large-area, physiological temperature sensors for multipoint measurements. *Proc. Natl. Acad. Sci. U.S.A.* **112**, 14533–14538 (2015).
12. T. Ohkuma, T. Ninomiya, H. Tomiyama, K. Kario, S. Hoshida, Y. Kita, T. Inoguchi, Y. Maeda, K. Kohara, Y. Tabara, M. Nakamura, T. Ohkubo, H. Watada, M. Munakata, M. Ohishi, N. Ito, M. Nakamura, T. Shoji, C. Vlachopoulos, A. Yamashina, M. Nagano, O. Yukiyo, T. Kabutoya, K. Asayama, N. Takashima, T. T. Chowdhury, K. Mitsuki-Shinohara, T. Yamashita, Brachial-ankle pulse wave velocity and the risk prediction of cardiovascular disease: An individual participant data meta-analysis. *Hypertension* **69**, 1045–1052 (2017).
13. J. Yang, J. Chen, Y. Su, Q. Jing, Z. Li, F. Yi, X. Wen, Z. Wang, Z. L. Wang, Eardrum-inspired active sensors for self-powered cardiovascular system characterization and throat-attached anti-interference voice recognition. *Adv. Mater.* **27**, 1316–1326 (2015).
14. D.-H. Kim, R. Ghaffari, N. Lu, S. Wang, S. P. Lee, H. Keum, R. D'Angelo, L. Klinker, Y. Su, C. Lu, Y.-S. Kim, A. Ameen, Y. Li, Y. Zhang, B. de Graff, Y.-Y. Hsu, Z. J. Liu, J. Ruskin, L. Xu, C. Lu, F. G. Omenetto, Y. Huang, M. Mansour, M. J. Slepian, J. A. Rogers, Electronic sensor and actuator webs for large-area complex geometry cardiac mapping and therapy. *Proc. Natl. Acad. Sci. U.S.A.* **109**, 19910–19915 (2012).
15. K. Meng, J. Chen, X. Li, Y. Wu, W. Fan, Z. Zhou, Q. He, X. Wang, X. Fan, Y. Zhang, J. Yang, Z. L. Wang, Flexible weaving constructed self-powered pressure sensor enabling continuous diagnosis of cardiovascular disease and measurement of cuffless blood pressure. *Adv. Funct. Mater.* **29**, 1806388 (2019).
16. B. Kraleman, M. Frühwirth, A. Píkovsky, M. Rosenblum, T. Kenner, J. Schaefer, M. Moser, In vivo cardiac phase response curve elucidates human respiratory heart rate variability. *Nat. Commun.* **4**, 2418 (2013).

17. X. Hui, E. C. Kan, Monitoring vital signs over multiplexed radio by near-field coherent sensing. *Nat. Electron.* **1**, 74–78 (2018).
18. Y. Ma, J. Choi, A. Hourlier-Fargette, Y. Xue, H. U. Chung, J. Y. Lee, X. Wang, Z. Xie, D. Kang, H. Wang, S. Han, S.-K. Kang, Y. Kang, X. Yu, M. J. Slepian, M. S. Raj, J. B. Model, X. Feng, R. Ghaffari, J. A. Rogers, Y. Huang, Relation between blood pressure and pulse wave velocity for human arteries. *Proc. Natl. Acad. Sci. U.S.A.* **115**, 11144–11149 (2018).
19. M. A. Saïd, R. N. Eppinga, E. Lipsic, N. Verweij, P. van der Harst, Relationship of arterial stiffness index and pulse pressure with cardiovascular disease and mortality. *J. Am. Heart Assoc.* **7**, e007621 (2018).
20. S. Xu, Y. Zhang, L. Jia, K. E. Mathewson, K.-I. Jang, J. Kim, H. Fu, X. Huang, P. Chava, R. Wang, S. Bhole, L. Wang, Y. J. Na, Y. Guan, M. Flavin, Z. Han, Y. Huang, J. A. Rogers, Soft microfluidic assemblies of sensors, circuits, and radios for the skin. *Science* **344**, 70–74 (2014).
21. S. Park, K. Fukuda, M. Wang, C. Lee, T. Yokota, H. Jin, H. Jinno, H. Kimura, P. Zalar, N. Matsuhisa, S. Umezue, G. C. Bazan, T. Someya, Ultraflexible near-infrared organic photodetectors for conformal photoplethysmogram sensors. *Adv. Mater.* **30**, 1802359 (2018).
22. S. Gong, W. Schwalb, Y. Wang, Y. Chen, Y. Tang, J. Si, B. Shirinzadeh, W. Cheng, A wearable and highly sensitive pressure sensor with ultrathin gold nanowires. *Nat. Commun.* **5**, 3132 (2014).
23. C. Dagdeviren, Y. Su, P. Joe, R. Yona, Y. Liu, Y.-S. Kim, Y. Huang, A. R. Damadoran, J. Xia, L. W. Martin, Y. Huang, J. A. Rogers, Conformable amplified lead zirconate titanate sensors with enhanced piezoelectric response for cutaneous pressure monitoring. *Nat. Commun.* **5**, 4496 (2014).
24. J. Park, M. Kim, Y. Lee, H. S. Lee, H. Ko, Fingertip skin-inspired microstructured ferroelectric skins discriminate static/dynamic pressure and temperature stimuli. *Sci. Adv.* **1**, e1500661 (2015).
25. Y. Zang, F. Zhang, D. Huang, X. Gao, C. Di, D. Zhu, Flexible suspended gate organic thin-film transistors for ultra-sensitive pressure detection. *Nat. Commun.* **6**, 6269 (2015).
26. Q. He, Y. Wu, Z. Feng, C. Sun, W. Fan, Z. Zhou, K. Meng, E. Fan, J. Yang, Triboelectric vibration sensor for a human-machine interface built on ubiquitous surfaces. *Nano Energy* **59**, 689–696 (2019).
27. G. Schwartz, B. C.-K. Tee, J. Mei, A. L. Appleton, D. H. Kim, H. Wang, Z. Bao, Flexible polymer transistors with high pressure sensitivity for application in electronic skin and health monitoring. *Nat. Commun.* **4**, 1859 (2013).
28. I. Graz, M. Kaltenbrunner, C. Keplinger, R. Schwödlauer, S. Bauer, S. P. Lacour, S. Wagner, Flexible ferroelectric field-effect transistor for large-area sensor skins and microphones. *Appl. Phys. Lett.* **89**, 073501 (2006).
29. X. He, Y. Zi, H. Guo, H. Zheng, Y. Xi, C. Wu, J. Wang, W. Zhang, C. Lu, Z. L. Wang, A highly stretchable fiber-based triboelectric nanogenerator for self-powered wearable electronics. *Adv. Funct. Mater.* **27**, 1604378 (2017).
30. A. Atalay, V. Sanchez, O. Atalay, D. M. Vogt, F. Haufe, R. J. Wood, C. J. Walsh, Batch fabrication of customizable silicone-textile composite capacitive strain sensors for human motion tracking. *Adv. Mater. Technol.* **2**, 1700136 (2017).
31. J. Lee, H. Kwon, J. Seo, S. Shin, J. H. Koo, C. Pang, S. Son, J. H. Kim, Y. H. Jang, D. E. Kim, T. Lee, Conductive fiber-based ultrasensitive textile pressure sensor for wearable electronics. *Adv. Mater.* **27**, 2433–2439 (2015).
32. W. B. Ko, D. S. Choi, C. H. Lee, J. Y. Yang, G. S. Yoon, J. P. Hong, Hierarchically nanostructured 1D conductive bundle yarn-based triboelectric nanogenerators. *Adv. Mater.* **29**, 1704434 (2017).
33. Z. Zhao, C. Yan, Z. Liu, X. Fu, L.-M. Peng, Y. Hu, Z. Zheng, Machine-washable textile triboelectric nanogenerators for effective human respiratory monitoring through loom weaving of metallic yarns. *Adv. Mater.* **28**, 10267–10274 (2016).
34. J. Chen, Y. Huang, N. Zhang, H. Zou, R. Liu, C. Tao, X. Fan, Z. L. Wang, Micro-cable structured textile for simultaneously harvesting solar and mechanical energy. *Nat. Energy* **1**, 16138 (2016).
35. J. Xiong, P. Cui, X. Chen, J. Wang, K. Parida, M.-F. Lin, P. S. Lee, Skin-touch-actuated textile-based triboelectric nanogenerator with black phosphorus for durable biomechanical energy harvesting. *Nat. Commun.* **9**, 4280 (2018).
36. L. Liu, Y. Yu, C. Yan, K. Li, Z. Zheng, Wearable energy-dense and power-dense supercapacitor yarns enabled by scalable graphene-metallic textile composite electrodes. *Nat. Commun.* **6**, 7260 (2015).
37. X. Pu, W. Song, M. Liu, C. Sun, C. Du, C. Jiang, X. Huang, D. Zou, W. Hu, Z. L. Wang, Wearable power-textiles by integrating fabric triboelectric nanogenerators and fiber-shaped dye-sensitized solar cells. *Adv. Energy Mater.* **6**, 1601048 (2016).
38. X. Pu, L. Li, M. Liu, C. Jiang, C. Du, Z. Zhao, W. Hu, Z. L. Wang, Wearable self-charging power textile based on flexible yarn supercapacitors and fabric nanogenerators. *Adv. Mater.* **28**, 98–105 (2016).
39. O. Atalay, W. R. Kennon, E. Demirok, Weft-knitted strain sensor for monitoring respiratory rate and its electro-mechanical modeling. *IEEE Sens. J.* **15**, 110–122 (2015).
40. S. Chen, S. Liu, P. Wang, H. Liu, L. Liu, Highly stretchable fiber-shaped e-textiles for strain/pressure sensing, full-range human motions detection, health monitoring, and 2D force mapping. *J. Mater. Sci.* **53**, 2995–3005 (2018).
41. M. Liu, X. Pu, C. Jiang, T. Liu, X. Huang, L. Chen, C. Du, J. Sun, W. Hu, Z. L. Wang, Large-area all-textile pressure sensors for monitoring human motion and physiological signals. *Adv. Mater.* **29**, 1703700 (2017).
42. C. Massaroni, C. Venanzi, A. P. Silvatti, D. Lo Presti, P. Saccomandi, D. Formica, F. Giurazza, M. A. Caponero, E. Schena, Smart textile for respiratory monitoring and thoraco-abdominal motion pattern evaluation. *J. Biophotonics* **11**, e201700263 (2018).
43. N. Luo, J. Zhang, X. Ding, Z. Zhou, Q. Zhang, Y.-T. Zhang, S.-C. Chen, J.-L. Hu, N. Zhao, Textile-enabled highly reproducible flexible pressure sensors for cardiovascular monitoring. *Adv. Mater. Technol.* **3**, 1700222 (2018).
44. W. W. Nichols, Clinical measurement of arterial stiffness obtained from noninvasive pressure waveforms. *Am. J. Hypertens.* **18**, 35–105 (2005).
45. X. Han, X. Chen, X. Tang, Y.-L. Chen, J.-H. Liu, Q.-D. Shen, Flexible polymer transducers for dynamic recognizing physiological signals. *Adv. Funct. Mater.* **26**, 3640–3648 (2016).
46. C. Wang, X. Li, H. Hu, L. Zhang, Z. Huang, M. Lin, Z. Zhang, Z. Yin, B. Huang, H. Gong, S. Bhaskaran, Y. Gu, M. Makihata, Y. Guo, Y. Lei, Y. Chen, C. Wang, Y. Li, T. Zhang, Z. Chen, A. P. Pisano, L. Zhang, Q. Zhou, S. Xu, Monitoring of the central blood pressure waveform via a conformal ultrasonic device. *Nat. Biomed. Eng.* **2**, 687–695 (2018).
47. S. Y. Hong, J. H. Oh, H. Park, J. Y. Yun, S. W. Jin, L. Sun, G. Zi, J. S. Ha, Polyurethane foam coated with a multi-walled carbon nanotube/polyaniline nanocomposite for a skin-like stretchable array of multi-functional sensors. *NPG Asia Mater.* **9**, e448 (2017).
48. R. Kelly, C. Hayward, A. Avolio, M. O'Rourke, Noninvasive determination of age-related changes in the human arterial pulse. *Circulation* **80**, 1652–1659 (1989).
49. G. Parati, C. Lombardi, F. Castagna, P. Mattaliano, P. P. Filardi, P. Agostoni; On behalf of the Italian Society of Cardiology (SIC) Working Group on Heart Failure members, Heart failure and sleep disorders. *Nat. Rev. Cardiol.* **13**, 389–403 (2016).

Acknowledgments

Funding: This work was supported by the National Natural Science Foundation of China (grant no. 51675069), the Fundamental Research Funds for the Central Universities (grant nos. 2018CDQYGD0020 and cqu2018CDHB1A05), the Scientific and Technological Research Program of Chongqing Municipal Education Commission (KJ1703047), and the National Science Foundation Projects of CQ (cstc2017shmsA40018 and cstc2018jcyjAX0076). **Author contributions:** W.F., J.Y., and Z.L.W. conceived the idea and designed the experiments. W.F., J.Y., and Z.L.W. performed the experiments with the assistance of Q.H., K.M., X.T., Z.Z., and G.Z. W.F., J.Y., and Z.L.W. organized the figures and wrote the manuscript. J.Y. and Z.L.W. supervised the project. All authors commented on the manuscript. **Competing interests:** The authors declare that they have no competing interests. **Data and materials availability:** All data needed to evaluate the conclusions in the paper are present in the paper and/or the Supplementary Materials. Additional data related to this paper may be requested from the authors.

Submitted 6 June 2019

Accepted 17 December 2019

Published 13 March 2020

10.1126/sciadv.aay2840

Citation: Wan, F., Q. He, K. Meng, X. Tan, Z. Zhou, G. Zhang, J. Yang, Z. L. Wang, Machine-knitted washable sensor array textile for precise epidermal physiological signal monitoring. *Sci. Adv.* **6**, eaay2840 (2020).